UV-Assisted Three-Dimensional Printing of Polymer Nanocomposites Based on Inorganic Fillers

Giovanni Postiglione, Gabriele Natale, Gianmarco Griffini, Marinella Levi, Stefano Turri
Department of Chemistry, Materials and Chemical Engineering "Giulio Natta", Politecnico di Milano, Milan, Italy

INTRODUCTION

Polymer-based nanocomposites have been studied extensively in the last decades as a means to achieve improved thermal, mechanical, optical, magnetic, and barrier properties in the resulting material *via* the control of the interactions between the polymeric host and the nanostructured filler [1–5]. Currently, great efforts are being produced in the attempt to develop new nanocomposite processing techniques that may allow the production of highly reliable and precise three-dimensional (3D) microdevices [6]. Stereolithography, two-photon polymerization, multijet modeling, and digital light processing represent some of the most explored techniques used for the fabrication of such microdevices that make use of photopolymerizable resins to achieve spatial resolutions that can approach 100 nm [7, 8].

Besides these relatively consolidated microfabrication technologies, a very promising and potentially cost-effective approach to manufacture such microdevices is represented by 3D printing, which consists in the direct fabrication of a 3D object starting from a digital model. 3D printing is now being used routinely in a variety of manufacturing sectors ranging from aerospace and automotive to bioengineering [9, 10]. An interesting evolution of the 3D printing technology is represented by ultraviolet-assisted 3D (UV-3D) printing, which allows the manufacturing of microdevices with 3D freeform or supported features starting from a photocurable polymeric material [11]. This technology consists of a computer-controlled microextrusion apparatus to which a source of UV light is applied. Upon UV light exposure, the extruded photocurable material undergoes a crosslinking process which gives instant rigidity to the extruded filament, thereby enabling the creation of multidirectional self-supported shapes along the trajectory of the extrusion point. In the last few years, the use of UV-3D printing has allowed the fabrication of polymer-based conductive microstructures, sensors, and electrical components by addition of conductive organic nanofillers such as carbon nanotubes into the polymeric matrix [12–16]. In addition, it has been recently demonstrated that by fine-tuning UV-3D printing processing parameters such as the extrusion nozzle speed, the material flow rate, and the intensity and position of the UV source according to the rheological properties of the photocurable resin, the fabrication of microcoils in a freeform manner can be made possible [17].

While most of the works on UV-3D printing have been mainly focused on the fabrication of free-standing or spanning micro-features embedding conductive

Correspondence to: Gianmarco Griffini; e-mail: gianmarco.griffini@polimi.it

nanofillers to impart electrical functionalities [11–15], very little is known about the effect of the addition of inorganic fillers into the photocurable resin on the rheological and mechanical properties of the resulting UV-3D printed nanocomposite material. Clearly, this information would provide a greater insight into the UV-3D printing process, thus allowing to widen the material selection and potentially improve further the mechanical properties of the 3D printed microstructure. Moreover, the effect of 3D printing direction, fill density (infill), and fill pattern on the mechanical properties of UV-3D printed microstructures has not been thoroughly investigated in the literature to date, being the vast majority of the studies on this topic mainly focused on more traditional 3D printing techniques such as fused deposition modeling (FDM) based on thermoplastic materials [18, 19]. In particular, the fabrication of cellular nanocomposites *via* UV-3D printing and the evaluation of their mechanical properties for different printing patterns and different reinforcing fillers have not been demonstrated in the literature to date, notwithstanding the enormous potential of these systems as light-weight highly performing structural materials [20].

In the effort to address these issues, a systematic investigation on the effect of the addition of different inorganic fillers on the rheological and mechanical properties of polymer-based nanocomposites for UV-3D printing is presented in this work. In particular, the rheological response of nanocomposite dispersions based on a solvent-free UV-curable resin loaded with different types of inorganic fillers is experimentally investigated at varying filler content. The fillers employed in this work are two different types of silica characterized by different specific surface areas and a montmorillonite-based nanoclay. Following such rheological characterization, optimal printability parameters for these systems are identified based on the shear rate of the materials at the extrusion nozzle. In addition, photocalorimetric measurements are used to assess the effect of the presence of the inorganic fillers on the thermodynamics and kinetics of the photocuring process of the resins. Moreover, by direct deposition of homogeneous solvent-free nanocomposite dispersions of filler in the UV-curable matrix, the effect of UV-3D printing direction, infill density, and fill pattern on the mechanical properties of UV-3D printed specimens is investigated by means of uniaxial tensile tests. Finally, examples of 3D macrostructures and microstructures directly formed upon UV-3D printing of such dispersions are reproducibly obtained and demonstrated, with a maximum spatial resolution approaching 200 μm.

EXPERIMENTAL

Materials

Fumed silica (specific surface area 50 m^2/g, primary particle size distribution range 10–100 nm) was purchased from Evonik Industries, Germany (Aerosil®OX50, OX50). Dichloromethane (DCM), fumed silica OX200 (200 m^2/g, primary particle size distribution 8–20 nm), and the photoinitiator 2-hydroxy-2-methyl-1-phenyl-propan-1-one (Darocur®1173, DAR) were purchased from Sigma-Aldrich, Italy. Trimethylolpropane ethoxylate triacrylate (TMPETA, average M_n ~560) was kindly provided by Arkema, while the nanoclay (Dellite® 43B, 6–8 μm characteristic length, D43B) was obtained from Laviosa Chimica Mineraria, Italy. All products were used as received.

Nanocomposite Dispersions

For the preparation of the nanocomposite dispersions at increasing filler concentration, a 3 wt% stock solution of DAR in TMPETA was prepared under magnetic stirring at room temperature for 30 min. Two different procedures were followed for dispersing fumed silica and dellite into the DAR/TMPETA stock solution. For silica compounds, the desired amount of OX200 or OX50 (ranging from 5 wt% to 15 wt% for OX200 and from 15 wt% to 30 wt% for OX50) was slowly added to the DAR/TMPETA solution, which was manually mixed until homogenization. The nanoclay dispersions were prepared by mixing the desired amount of D43B in DCM so as to obtain a 0.01 w/w dispersion. After 10 min magnetic stirring at 500 rpm, the solution was ultrasonicated for 45 min with a Sonic & Materials VCX130 sonicator tip. This last step was carried out in an ice bath to prevent DCM evaporation and to minimize undesired exothermic phenomena resulting from the ultrasonication process. Finally, the proper amount of DAR/TMPETA solution was added to the D43B dispersion and the solvent was evaporated under a fume hood. Four dispersions of D43B in DAR/TMPETA at D43B concentrations ranging from 3 wt% to 15 wt% were prepared.

Characterization Techniques

The rheological characterization of the nanocomposite dispersions at increasing filler concentration was performed using a Rheometrics DSR200 rheometer with a 25 mm plate-cone configuration at 25°C. Steady shear tests on the DAR/TMPETA dispersions were performed for 3 min in the 0–4500 Pa range.

Photocalorimetric measurements were performed on a DSC/823e (Mettler Toledo) coupled to a fiber-guided UV light source generated by a medium-pressure mercury lamp (Lightningcure LC8, Hamamatsu) in the 300–450 nm wavelength range at an intensity of 15 mW/cm^2. Nanocomposite samples (5 mg, 500 μm thickness) were placed into an open aluminum crucible and exposed to such UV light at 25°C under nitrogen flow (50 mL/min). The heat of reaction was obtained by integration of the resulting exotherms.

Optical microscopy was employed to evaluate the microstructural features of the UV-3D printed architectures

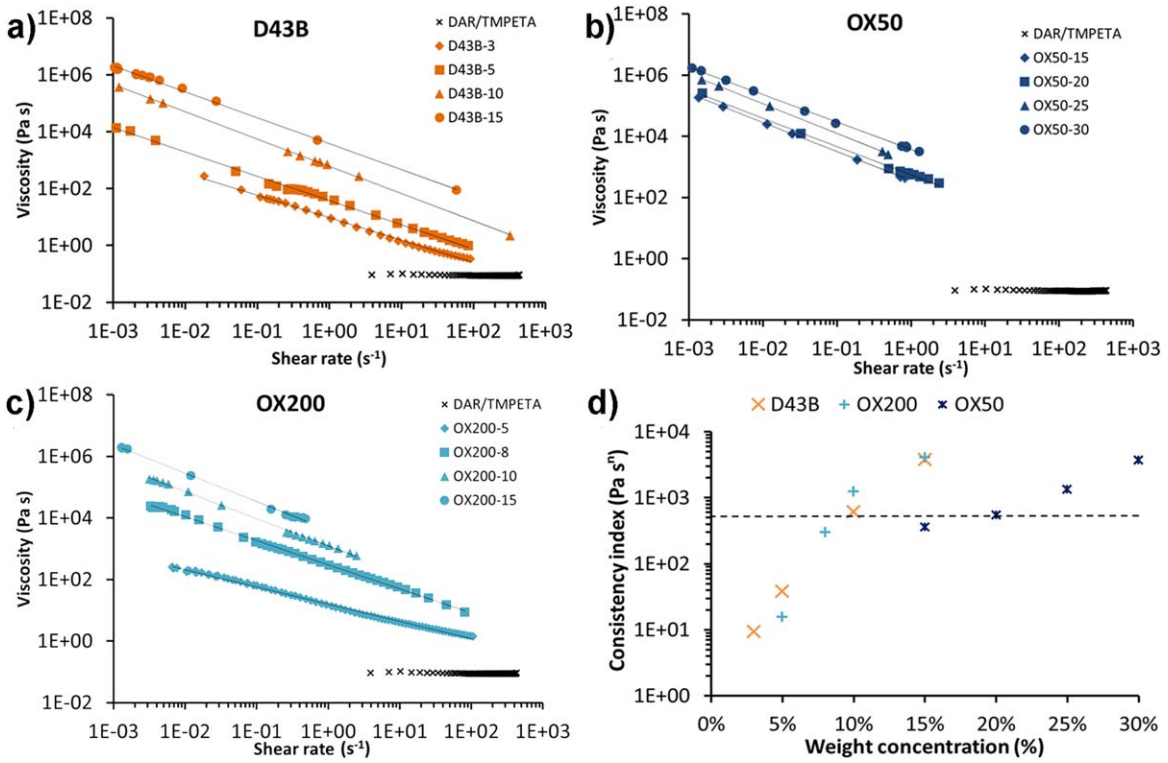

FIG. 1. Viscosity curves of (a) D43B, (b) OX50, (c) OX200 formulations at different filler concentrations. (d) Corresponding consistency indexes K as a function of filler concentration. [Color figure can be viewed in the online issue, which is available at wileyonlinelibrary.com.]

using an Olympus BX-60 reflected-light optical microscope with bright-field (BF) and dark-field (DF) imaging and a SZ-CTV Olympus stereoscopic microscope both equipped with an Infinity 2 digital camera.

Scanning electron microscopy (SEM) was performed on UV-3D printed nanocomposite-based microstructures with a Carl Zeiss EVO 50 Extended pressure scanning electron microscope (acceleration voltage of 15.00–17.50 kV) to evaluate their surface morphology and the 3D architecture. SEM analysis with energy-dispersive X-ray spectroscopy (EDS) on cryo-fractured samples was performed to evaluate the quality of filler dispersion into the polymer matrix.

A low-cost home-assembled 3Drag 1.2 benchtop printer (Futura Elettronica, Italy) incorporating a syringe dispenser equipped with five low-power UV light emitting diodes (LEDs) with light emission peaked at 365 nm and a viewing angle of 20–25° (Aftertech SAS, Italy) was used for UV-3D printing of the nanocomposite microstructures (see Supporting Information). Print speed and nozzle diameter ranged between 0.1–30 mm/s and 0.2–1.5 mm, respectively.

Tensile tests were performed on cast and UV-3D printed dumbbell specimens (narrow section 3 mm × 5mm× 20 mm) at 1 mm/min testing speed on a Zwick-Roell Z010 with a 10 kN load cell and a longstroke extensometer following the American Society for Testing and Materials (ASTM) D638 standard. The specimens with reduced infill density had a 3 mm × 13 mm × 50 mm narrow section. UV-3D printed specimens were obtained by operating the 3D printer at 7 mm/s with a 0.51 mm nozzle. At least three specimens of each type were tested.

RESULTS AND DISCUSSION

In order to ensure optimal printability of the liquid nanocomposite dispersions into stable 3D solid structures at the printing nozzle exit, their rheological behavior needs to be comprehensively investigated. To this end, the viscosity of nanocomposite dispersions based on DAR/TMPETA and increasing concentrations of D43B, OX50, and OX200 was determined by isothermal cone-plate rheological measurements. Figure 1a–c shows the plots of DAR/TMPETA viscosity as a function of shear rate at different filler concentrations (the name of the sample is identified by the acronym indicating the type of filler used, followed by a number indicating the filler concentration as wt%). Four different concentrations were selected for each filler type, so that the viscosity of the resulting polymer composite dispersion was suitable for processing in the UV-3DP apparatus presented in this work. In order to allow for comparisons, the plot of viscosity vs. shear rate for the unloaded DAR/TMPETA resin is also presented. As expected, the pristine resin shows a typical Newtonian behavior, characterized by a constant viscosity for increasing shear-rate values ($\eta \approx$ 0.09 Pa s in the 3–5 10^2 1/s shear-rate interval).

As opposed to this, all nanocomposite dispersions clearly exhibit a typical shear-thinning response characterized by decreasing viscosity with increasing shear rate, indicating

that both fumed silica and dellite strongly interact with the polymer matrix. Such rheological behavior is highly desirable as it allows to enhance the nanocomposite processability through the capillary extrusion nozzle due to the decreased viscosity of the material under the high shear-rate characteristics of the 3D printing process. As shown in the plots, the viscosity curves of all formulations can be very well fitted with a power–law fluid relationship according to the following equation:

$$\eta = K\dot{\gamma}^{n-1} \tag{1}$$

The values of the coefficients calculated by means of the power–law equation (consistency index K and power–law index n) were used to compare the rheological response of the different nanocomposite formulations (see Supporting Information). In particular, the power–law index n is related to the slope of the viscosity curve and can therefore provide an indication on the extent of shear-thinning character given to the UV-curable resin by the presence of the inorganic filler. Conversely, the consistency index K gives an indication of the viscosity of the specific formulation at shear rate of 1 1/s. Due to their shear-thinning behavior, all formulations present power–law indexes $n < 1$ with values slightly higher for the systems with filler concentration below 10 wt% (OX200-5, OX200-8, D43B-3, and D43B-5), likely ascribable to the weaker polymer–filler interactions arising in lightly loaded systems. Conversely, the consistency index K is found to be greatly affected by the concentration and type of inorganic filler. As shown in Fig. 1d where K values calculated for the different nanocomposite formulations by means of *Eq. 1* are plotted as a function of filler concentration, a significantly lower increase in filler concentration gives rise to a much sharper increase of consistency index K in the case of OX200 as compared to OX50. In particular, while an over-two-order-of-magnitude increase in K is observed for OX200 when its concentration in the formulation is increased from 5 wt% to 15 wt%, the progressive addition of OX50 to the DAR/TMPETA system in the 15–30 wt% range only results in a tenfold increase in K. These trends can be explained by considering that OX200 fumed silica is characterized by a larger specific surface area than OX50 (200 g/m^2 vs. 50 g/m^2, respectively) that is responsible for stronger interactions between the inorganic filler and the polymer host matrix, leading to a more efficient viscosity increase on the UV-curable resin. As also evident from Fig. 1d, the addition of nanoclay filler D43B leads to a similar rheological response as that observed with OX200, likely indicating similar filler–polymer matrix interactions for D43B and OX200.

Based on the values of the consistency index K and the power-law index n for each formulation calculated from *Eq. 1*, it is possible to predict the rheological behavior of the nanocomposite dispersions within the 3D printer extruder using the capillary flow model [21, 22]. First, the apparent shear rate $\dot{\gamma}_{\mathrm{app}}$ of the fluid inside a capillary is determined from the Hagen–Poiseuille equation:

$$\dot{\gamma}_{app} = \frac{4Q}{\pi R^3} \tag{2}$$

where Q is the volumetric flow rate and R is the radius of the capillary. The actual shear rate $\dot{\gamma}$ can be derived using the well-known Mooney–Rabinowitch correction for non-Newtonian fluids (with n being the power-law index calculated from the power–law equation):

$$\dot{\gamma} = \dot{\gamma}_{app}\frac{3n+1}{4n} \tag{3}$$

Since the volumetric flow rate through the 3D printer nozzle can easily be calculated from the printing speed and nozzle cross section, an allowable process related shear rate interval can be determined for a given material by simply varying the 3D printing speed settings and the nozzle size (see exemplary calculation in the Supporting Information).

Following the theoretical approach presented above, the printability of all dispersions was also practically tested with the 3D printer (see Supporting Information). Despite the fact the all formulations could be extruded through the various nozzles employed in this work in good agreement with the previous calculations, only some of them showed good printability properties (Supporting Information). Indeed, in order to guarantee optimal printing resolution and well defined printed features, the extruded wet filament must retain its integrity right after its deposition onto the printing plate and prior to UV irradiation. Considering this requirement, experimental 3D printing tests (Supporting Information) showed that only formulations with sufficiently high consistency indexes ($K > 550$ Pa s^n) were found to exhibit optimal printability properties (this printability limit is represented in Fig. 1d as a dotted line).

In order to characterize the photopolymerization process of the UV-curable resin and the possible effect of the presence of the filler on the thermodynamics and the kinetics of the curing reaction, photocalorimetric measurements were performed on all nanocomposite formulations. The values of enthalpy of polymerization are shown in Fig. 2a as a function of filler type and concentration. In the plot, the measured heat (ΔH) of polymerization has been corrected considering the exact DAR/TMPETA weight fraction present in every formulations during the photocalorimetric scan. Clearly, the presence of the different inorganic fillers has no practical effect on the heat of polymerization of the nanocomposite, as in all cases a ΔH value of approximately 300 J/g is measured, similarly to what observed in unfilled DAR/TMPETA. Slightly lower ΔH values are found in OX200-8, OX200-10, OX200-15, and D43B-15 formulations, likely ascribable to the stronger filler–polymer matrix interactions

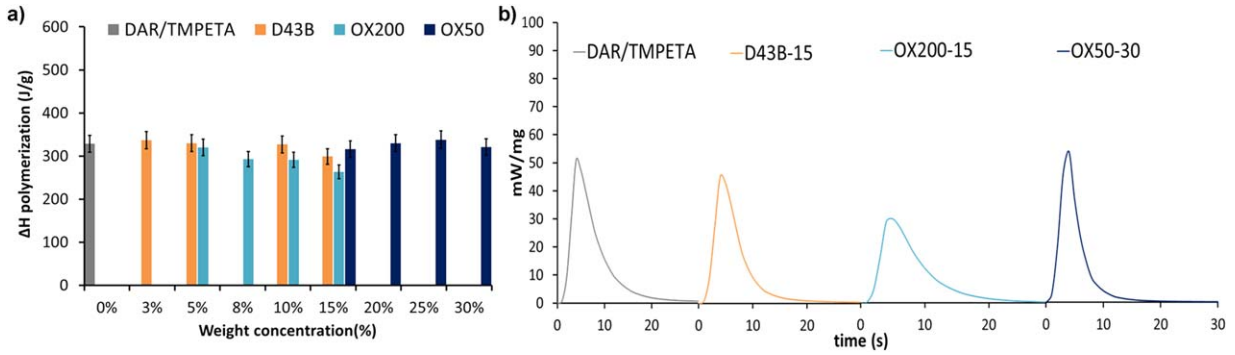

FIG. 2. (a) Enthalpy of photopolymerization of the UV-curable nanocomposites as a function of filler concentration and (b) photocalorimetric scans of the UV-curable resin TMPETA/DAR and of the polymer-based UV-curable nanocomposites with different filler types. [Color figure can be viewed in the online issue, which is available at wileyonlinelibrary.com.]

occurring for these high specific surface area fillers at such high concentrations that may partially hinder polymer chain growth during the photopolymerization reaction. However, such counteracting effect is relatively limited, as even for the formulation exhibiting the lowest value of measured heat of polymerization (OX200-15), the conversion of the UV-curing reaction (calculated as the ratio between the enthalpy of reaction for the nanocomposite formulation and the enthalpy of reaction for the unfilled resin) is over 80%. As opposed to OX200-based and D43B-based nanocomposite systems, no effect on the UV-curing thermodynamics is observed for OX50 nanocomposites, irrespective of filler concentration.

In the attempt to investigate the effect of filler type and concentration on the photopolymerization kinetics of the DAR/TMPETA resin, the photocalorimetric scans of resin formulations based on different fillers (D43B, OX200, and OX50) were compared with the photocalorimetric scan of unfilled DAR/TMPETA. Figure 2b reports the results for the resin formulations based on the three different fillers at the highest filler concentration examined in this work (D43B-15, OX200-15, and OX50-30). As shown in the plot, all filled systems present similar polymerization kinetics, comparable to what found for the unfilled DAR/TMPETA resin, with the exothermic peak of polymerization found after 4 s from the beginning of the UV exposure. These results clearly indicate that the presence of the filler does not alter significantly the curing speed of the polymer-based nanocomposite at the filler concentrations investigated in this work (which are suitable for 3D printing purposes), thus enabling an effective UV-3D printing process *via* the rapid UV-induced polymerization of the extruded nanocomposite wet filament. This represents a very favorable feature in view of the UV-3D printing fabrication process of these polymer-based nanocomposite formulations. Indeed, the material flowing out from the extrusion nozzle can be polymerized rapidly enough to withstand the subsequent deposition of additional layers of materials without collapsing and to potentially allow for the production of spanning features. Additionally, the filler concentration in the UV-curable resin may be tuned in such a way that desirable physical characteristics of the system such as the initial nanocomposite fluid viscosity or the mechanical properties of the final 3D printed material may be independently optimized without significantly affecting the UV-curing reaction.

In order to investigate the mechanical response of the nanocomposites with different filler types, dumbbell specimens were UV-3D printed and assessed by means of uniaxial tensile testing. According to the outcomes of the rheological characterization presented in Fig. 1, formulations containing the minimum allowable amount of filler to enable optimal UV-3D printing were selected for the mechanical tests, namely D43B-10, OX50-20, and OX200-10 (i.e., nanocomposite formulations with the lowest filler concentration giving consistency index values K above the printability threshold value represented by the dotted line in Fig. 1d). In addition, to evaluate the effect of the filament printing direction on the mechanical properties of the UV-3D printed structures, specimens were fabricated by UV-3D printing both along the longitudinal axis (90° in Fig. 3) and with a 45° mesh-type pattern (45° in Fig. 3). All UV-3D printed specimens were fabricated at the maximum filling density (100% *infill*) and their mechanical response was compared with that obtained from OX50-20 and OX200-10 samples realized by mold casting. It is worth noting that after UV-3D printing all samples achieved a nearly 100% crosslinking conversion, as evidenced by the negligible residual exothermic heat of reaction observed on UV-3D printed samples measured by photocalorimetric experiments (see Supporting Information).

D43B-10 cast specimens could not be produced due to incomplete polymerization of such samples likely originating from the UV-shielding effect of the nanoclay-based filler that partially hampers UV light from being absorbed by the DAR photoinitiator and prevents it from being efficiently used for the UV-curing reaction. Such UV-shielding effect is more pronounced for larger sample thicknesses as in the case of D43B-10 cast specimens (3 mm thick), while it is relatively negligible in the case of the thin wet filaments (0.2–0.84 mm nozzle diameter) characteristic of the UV-3D printing process.

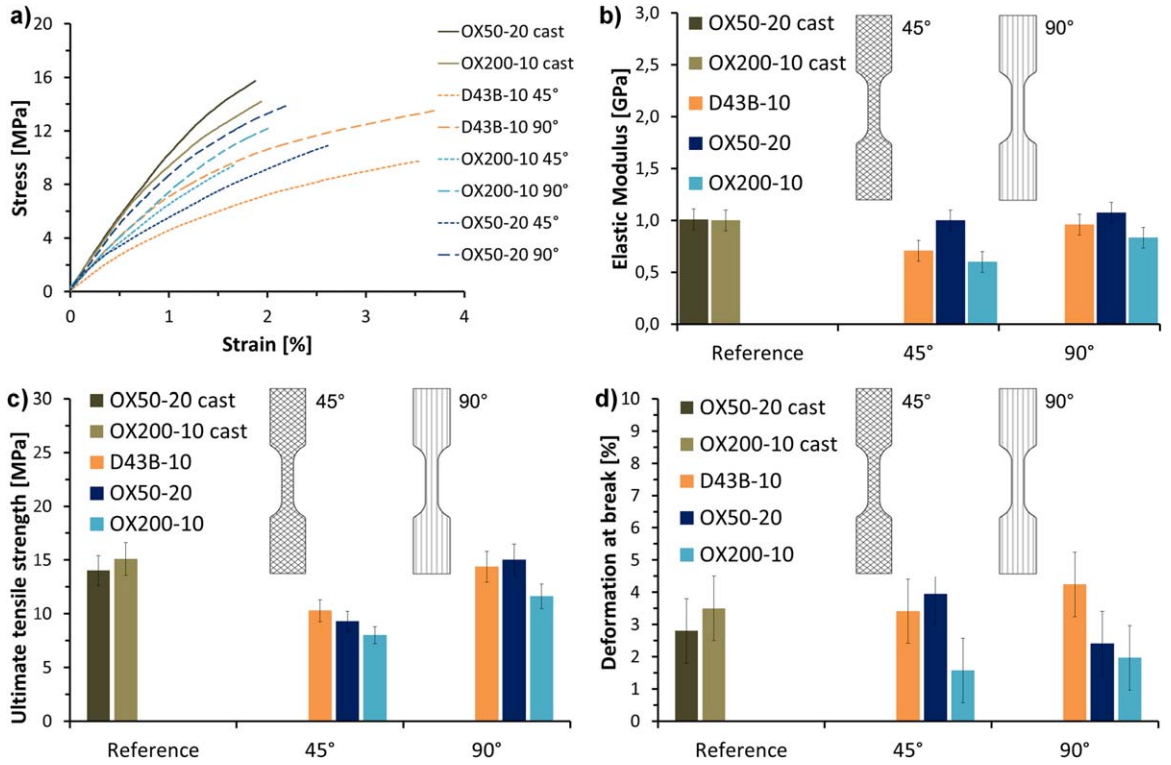

FIG. 3. (a) Representative stress–strain curves of UV-3D printed and cast samples; average values of (b) elastic modulus, (c) ultimate tensile strength, and (d) deformation at break. [Color figure can be viewed in the online issue, which is available at wileyonlinelibrary.com.]

Representative stress–strain curves for the samples investigated here are presented in Fig. 3a, while the average values of elastic modulus, ultimate tensile strength, and deformation at break obtained from the tensile tests on such samples are plotted in Fig. 3b–d, respectively. As evident from Fig. 3b, the elastic modulus of the OX50-20 UV-3D printed nanocomposite is comparable with that found for the corresponding cast sample and lies in the 1 GPa range, irrespective of the printing direction employed (45° and 90° printing pattern). As opposed to this, slightly lower values of elastic modulus are reported for OX200-10 UV-3D printed nanocomposites with respect to the homologous cast samples. In addition, D43B-10 materials exhibit elastic modulus values in line with those found in OX200-10 samples. As presented in Fig. 3b and c, the UV-3D printed samples with 90° printing pattern show a slight increase in elastic modulus and ultimate tensile strength compared to samples printed with a 45° printing pattern irrespective of the type of filler employed. In particular, values of ultimate tensile strength comparable to those found for cast samples are obtained in OX50-20, OX200-10, and D43B-10 samples printed with a 90° pattern (15 MPa range), while the corresponding samples printed with a 45° pattern are characterized by lower ultimate tensile strength values in the range between 7 and 10 MPa. These results suggest that the UV-3D printing process potentially allows for customized control of the mechanical properties of the UV-3D printed object by simple modification of the printing direction. Interestingly, all UV-3D printed samples show values of deformation at break in the 2–4% range which are in close agreement with those obtained from the control cast samples, independently from the printing direction. Only OX200-10/90° nanocomposites seems to give lower deformation at break values, although this may not be statistically significant given the large standard deviations registered for these measurements. It is worth highlighting that the quality of the dispersion of the filler into the polymer matrix was also evaluated by means of SEM analysis on printed nanocomposites at varying filler type (see Supporting Information). By examination of the cryo-fractured surface of the printed nanocomposite samples, a good level of dispersion of the fillers into the UV-curable polymer matrix is found even at high filler loading, thus suggesting the absence of any noticeable agglomerates that may affect the mechanical properties of the final printed samples.

Thanks to the great design flexibility allowed by the UV-3D printing process, the fabrication of complex shapes with arbitrary patterns can be envisaged. Taking inspiration from the natural world [23], cellular specimens with different unit cell geometry (infill pattern) and increasing infill density were realized by UV-3D printing, as shown in Fig. 4a–f where zoomed optical stereoscopic images of the UV-3D printed samples clearly highlight the excellent resolution and printing accuracy achievable with the UV-3D printing setup assembled in this work. In particular, samples with squared and hexagonal networks with three different relative densities (from 0.37 to 0.51) were UV-3D printed from OX200-10 nanocomposite

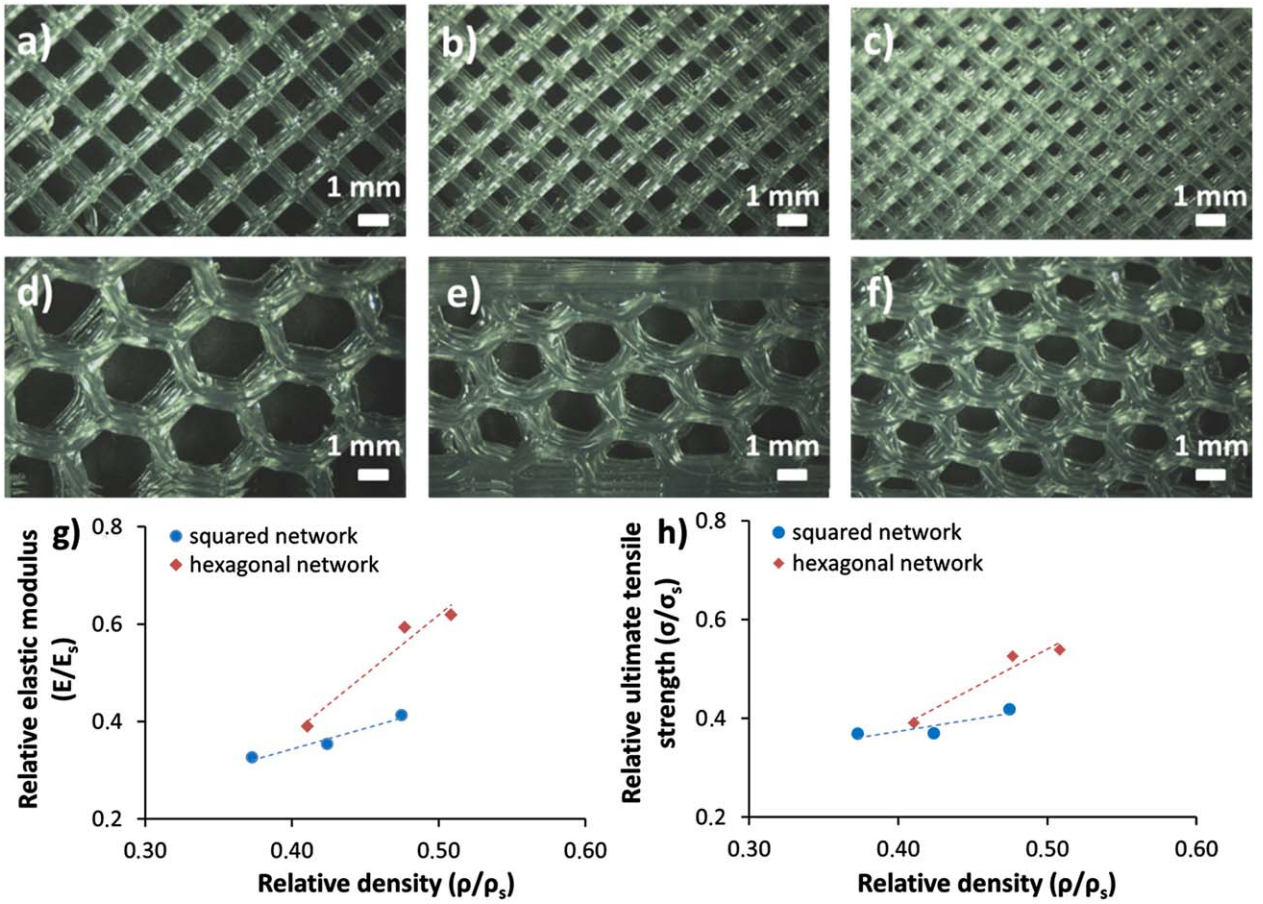

FIG. 4. Optical stereoscopic images of the UV-3D printed specimens with (a–c) squared unit cell and (d–f) hexagonal unit cell at increasing infill density. Plots of (g) the relative elastic modulus and (h) relative ultimate tensile strength as a function of the relative density of the specimens. Dotted lines are a guide for the eye. [Color figure can be viewed in the online issue, which is available at wileyonlinelibrary.com.]

formulation and mechanically characterized by means of uniaxial tensile tests. Plots of the relative elastic modulus E/E_s and the relative ultimate tensile strength σ/σ_s as a function of the relative density ρ/ρ_s are presented in Fig. 4g and h, where E_s, σ_s, and ρ_s refer to the elastic modulus, tensile strength, and density of the OX200-10 solid material, while E, σ, and ρ are the elastic modulus, tensile strength, and density of the OX200-10 cellular specimen. Both the relative elastic modulus and the relative ultimate tensile strength are found to increase at increasing relative density irrespective of the unit cell geometry. This trend is in line with the fact that for increasing relative densities, the mechanical behavior of the cellular specimen approaches that of the solid material ($\rho/\rho_s = 1$). Furthermore, the hexagonal unit cell is found to yield higher mechanical properties compared to the square unit cell for comparable values of relative densities, both in the case of the elastic modulus and the ultimate tensile strength. These results are in agreement with the typical mechanical behavior of cellular materials [24].

These observations lead to the conclusion that the filling pattern takes on a fundamental role in determining the final mechanical properties of the UV-3D printed objects, further highlighting the ability of UV-3D printing to modulate the mechanical behavior of the printed material in a relatively simple, straightforward and versatile fashion.

In order to demonstrate the potential of UV-3D printing in processing the nanocomposite dispersions developed in this work, different macrostructures and microstructures were fabricated using a low-cost benchtop 3D printer appropriately modified to accommodate a syringe dispenser feeding with the nanocomposite dispersions an extruding nozzle equipped with five low-power UV LEDs ($\lambda_{emission} = 365$ nm) (Fig. 5a and Supporting Information).

First, a woven-like microstructure was obtained by UV-3D printing two layers of OX200-10 nanocomposite formulation on top of each other at a printing speed of 20 mm/s. As shown in the optical micrograph presented in Fig. 5b, the filament extrusion resulted in planar solid features of approximately 200 μm average width. The same printing process parameters (printing speed 20 mm/s, layer height 0.1 mm) and nanocomposite dispersion (OX200-10) were used to fabricate a UV-3D printed six-layer matrix-like microstructure of approximately 600 μm

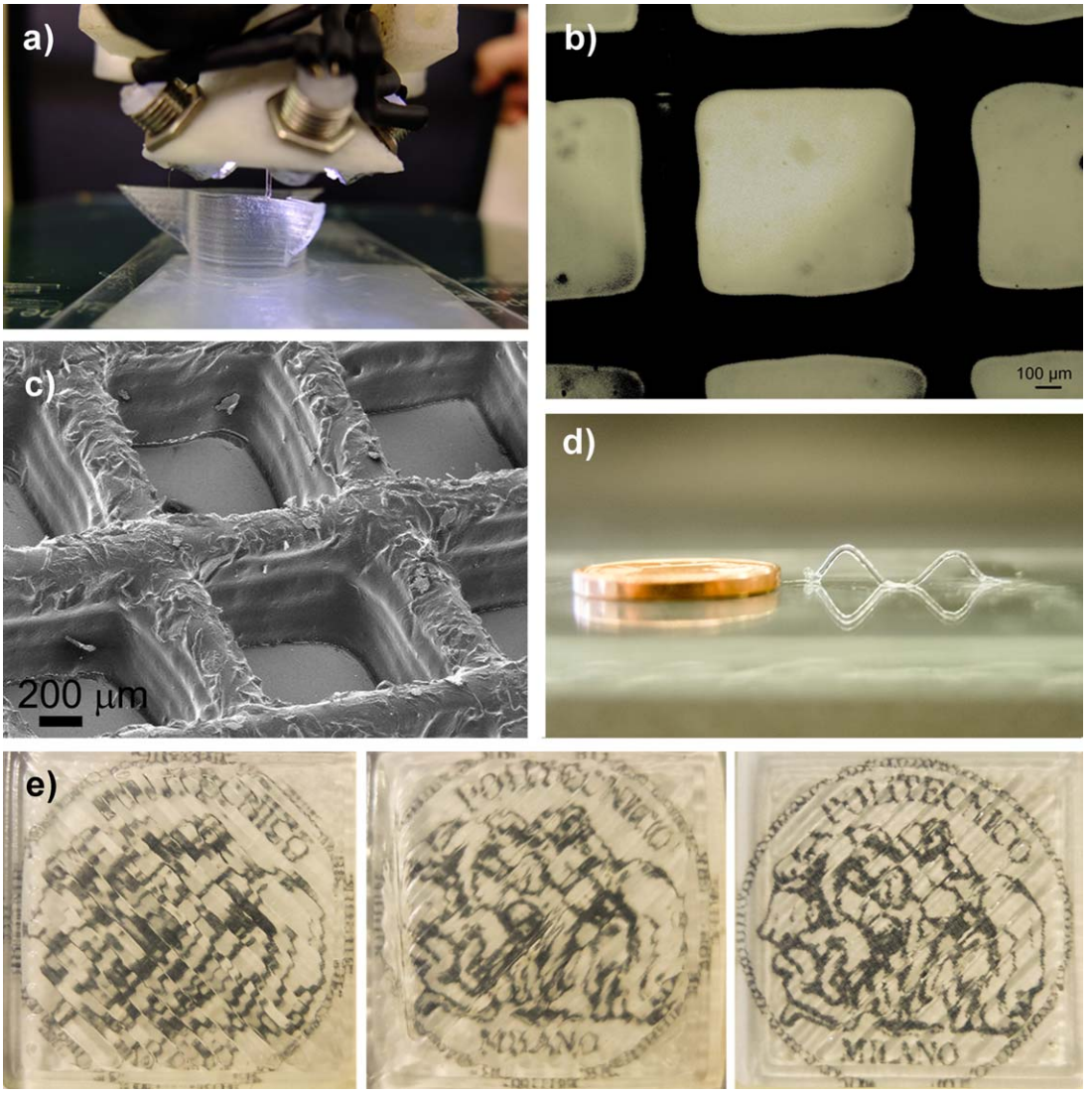

FIG. 5. (a) Optical image taken during the fabrication of a UV-3D printed macroscopic object; (b) optical image of a two-layer woven-like microstructure; (c) SEM image of a multilayer matrix-like microstructure; (d) UV-3D printed spanning features (a 1 cent euro coin is reported in the image for dimensional reference); and (e) translucent planar structures of increasing transparency obtained by UV-3D printing the nanocomposite dispersion with different layer-height settings. [Color figure can be viewed in the online issue, which is available at wileyonlinelibrary.com.]

height, 600 μm lateral size, and filament diameter of 200 μm (Fig. 5c). In addition, the UV-3D printing setup allowed to shift from the layer-by-layer deposition approach to obtain 3D freeform spanning features, as evident from Fig. 5d. In this case, OX200-10 system was employed at 3 mm/s, so as to be able to slow down the 3D printing process, induce rapid UV polymerization of the wet nanocomposite filament, and allow the formation of the spanning features that can cover a few millimeters in length without structural collapses. The fabrication of such 3D microstructures suggests the possibility to employ UV-3D printing to realize complex architectures and structural components at the microscale in a very versatile and straightforward fashion. As a further example of the high flexibility of the UV-3D printing approach combined with the nanocomposite materials presented in this work, macrostructures characterized by increasing levels of transparency/translucency were obtained using the OX200-10 nanocomposite formulation. As shown in Fig. 5e, by carefully controlling the UV-3D printing process parameters (layer height from 0.4 to 0.3 mm, printing speed 5 mm/s, infill density 100%, and nozzle diameter 0.84 mm), it was possible to produce translucent planar structures with varying degrees of optical transparency, suggesting the potential use of such customizable 3D systems in fields such as optics and optofluidics where optical clarity may represent a requirement. As a final demonstration of the potential of the nanocomposite dispersions developed in this work, examples of macroscopic UV-3D printed objects were also fabricated, with length scales in the cm range (Supporting Information), thereby giving a further practical demonstration of the direct applicability of this approach in the field of advanced additive manufacturing.

CONCLUSIONS

In conclusion, nanocomposites based on a UV-curable polymeric resin and different inorganic fillers were developed in this work for use in UV-3D printing applications. A rheological characterization of the nanocomposite dispersions at varying filler concentration was performed and optimal extrusion and printability parameters for these systems were identified based on the shear rate of the materials at the extrusion nozzle by applying classical power–law fluid relationships and the capillary flow model. Photocalorimetric measurements demonstrated that a very rapid (4 s) curing reaction could be achieved with these systems upon UV-light irradiation, and that the presence of the inorganic fillers did not affect the thermodynamics and kinetics of the UV-curing process of the polymeric matrix. The direct UV-3D printing of such homogeneous solvent-free polymer-based nanocomposite dispersions allowed to investigate the effect of printing direction, infill density, and fill pattern on the mechanical response of UV-3D printed specimens by uniaxial tensile tests. All samples exhibited excellent mechanical properties comparable to those found in the homologous casted materials. In addition, cellular nanocomposite materials were produced with hexagonal or squared unit cells that allowed to demonstrate the possibility to control the mechanical properties of the UV-3D printed materials by simply varying the infill design structure. Finally, examples of 3D macroarchitectures and microarchitectures, spanning features, and planar transparent structures directly formed upon UV-3D printing of such nanocomposite dispersions were reproducibly obtained and demonstrated, clearly highlighting the suitability of these polymeric materials for advanced UV-3D printing applications.

REFERENCES

1. P.M. Ajayan, L.S. Schadler, and P.V. Braun, *Nanocomposite Science and Technology*, Wiley-VCH, Weinheim (2003).
2. S. Kaur, M. Gallei, and E. Ionescu, *Adv. Polym. Sci.*, **267**, 143 (2015).
3. H. Althues, J. Henle, and S. Kaskel, *Chem. Soc. Rev.*, **36**, 1454 (2007).
4. A. Di Gianni, E. Amerio, O. Monticelli, and R. Bongiovanni, *Appl. Clay. Sci.*, **42**, 116 (2008).
5. S. Li, M.M. Lin, M.S. Toprak, D.K. Kim, and M. Muhammed, *Nano Rev.*, **1**, 5214 (2010).
6. M. Vaezi, H. Seitz, and S. Yang, *Int. J. Adv. Manuf. Technol.*, **67**, 1721 (2013).
7. I. Gibson, D.W. Rosen and B. Stucker, *Additive Manufacturing Technologies: Rapid Prototyping to Direct Digital Manufacturing*, Springer, New York (2010).
8. J.R. Tumbleston, D. Shirvanyants, N. Ermoshkin, R. Janusziewicz, A.R. Johnson, D. Kelly, K. Chen, R. Pinschmidt, J.P. Rolland, A. Ermoshkin, E.T. Samulski, and J.M. DeSimone, *Science*, **347**, 1349 (2015).
9. V. Petrovic, J.V. Haro Gonzalez, O. Jordá Ferrando, J. Delgado Gordillo, J.R. Blasco Puchades, and L. Portoles Griñan, *Int. J. Prod. Res.*, **49**, 1061 (2011).
10. B.C. Gross, J.L. Erkal, S.Y. Lockwood, C. Chen, and D.M. Spence, *Anal. Chem.*, **86**, 3240 (2014).
11. L.L. Lebel, B. Aïssa, M.A. El Khakani, and D. Therriault, *Adv. Mater.*, **22**, 592 (2010).
12. R.D. Farahani, H. Dalir, V. Le Borgne, L.A. Gautier, M.A. El Khakani, M. Lévesque, and D. Therriault, *Nanotechnology*, **23**, 085502 (2012).
13. B. Aïssa, D. Therriault, R.D. Farahani, L.L. Lebel, and M.A. El Khakani, *Nanotechnology*, **23**, 115705 (2012).
14. L.L. Lebel, B. Aïssa, M.A. El Khakani, and D. Therriault, *Compos. Sci. Technol.*, **70**, 518 (2010).
15. G. Postiglione, G. Natale, G. Griffini, M. Levi, and S. Turri, *Composites Part A*, **76**, 110 (2015).
16. R.D. Farahani, H. Dalir, V. Le Borgne, L.A. Gautier, M.A. El Khakani, M. Lévesque, and D. Therriault, *Compos. Sci. Technol.*, **72**, 1387 (2012).
17. R.D. Farahani, L.L. Lebel, and D. Therriault, *J. Micromech. Microeng.*, **24**, 055020 (2014).
18. S. Ahn, M. Montero, D. Odell, S. Roundy, and P.K. Wright, *Rapid Prototyping J.*, **8**, 248 (2002).
19. B.M. Tymraka, M. Kreigerb, and J.M. Pearce, *Mater. Des*, **58**, 242 (2014).
20. B.G. Compton and J.A. Lewis, *Adv. Mater.*, **26**, 5930 (2014).
21. H.A. Barnes, J.F. Hutton, and K. Walters, *An Introduction to Rheology*, Elsevier, Amsterdam (1997).
22. J. Bruneaux, D. Therriault, and M. Heuzey, *J. Micromech. Microeng.*, **18**, 115020 (2008).
23. X. Xu, L. Heng, X. Zhao, J. Ma, L. Lin, and L. Jiang, *J. Mater. Chem.*, **22**, 10883 (2012).
24. M.F. Ashby, *Metall. Trans.*, **14A**, 1755 (1983).